(2)

AR-006-841

A VISAR Velocity Interferometer System at MRL for Slapper Detonator and Shockwave Studies

David J. Hatt

MRL Technical Report
MRL-TR-91-42

Abstract

This report describes the commissioning and appraisal of a conventional 3-detector VISAR velocity interferometer system (Systems, Science, and Software, Model 3SLVI-401) for measuring the velocity-time histories of small plastic flyer plates produced by exploding bridge foil generators.

Proper treatment of the flyer surface to diffusely reflect the laser beam was found to be important. Roughening the surface with a miniature grit-blaster produced the best results. Peak velocities in the range 1500 m/s to 3900 m/s were obtained for small- and medium-scale flyers (bridge widths of 0.25 mm and 1.5 mm, respectively). Accelerations were in the range 10 Gm/s^2 to 100 Gm/s^2. The uncertainty of the measurements was found to be related to the limited high-frequency response (less than 100 MHz) of the photodetectors.

After replacement of the original non-flat beamsplitter, the arms of the interferometer were not quite compensated. A modified VISAR velocity equation that allows for the effective etalon length of the λ/8 waveplate/beamsplitter combination is derived.

MATERIALS RESEARCH LABORATORY

Published by

Materials Research Laboratory
Cordite Avenue, Maribyrnong
Victoria, 3032 Australia

Telephone: (03) 319 3887
Fax: (03) 318 4536

AR No. 006-841

APPROVED FOR PUBLIC RELEASE

Author

David J. Hatt

David Hatt graduated Dip App Physics from the Ballarat School of Mines and Industries in 1968, and joined MRL in 1969. Until transferring to the Explosives Ordnance Division in 1977, he worked on Defence standards and calibration systems. In the Explosives Ordnance Division he has specialized in the development and application of instrumentation for the study of high-speed events and phenomena related to explosives and ammunition.

Contents

A VISAR Velocity Interferometer System at MRL for Slapper Detonator and Shockwave Studies

1. Introduction

Since its invention in 1972 [1], the VISAR (Velocity Interferometer System for Any Reflector) has found widespread use in explosives research laboratories around the world for velocity measurements of rapid surface motions (typically in the range 1 to 5 km/s). Quite often, large accelerations (10 to 200 Gm/s^2) are associated with producing these velocities. The VISAR and the Fabry-Perot interferometer [2] are virtually the only diagnostic tools available for obtaining accurate continuous velocity-time histories for such surface motions. One particular application is for studying the performance of flyers generated by exploding bridge foil devices, such as those used in slapper detonators [3] and flyer generators used for shocked material studies [4, 5].

Establishment of a VISAR capabilitity at MRL was facilitated by the loan of VISAR components from Eglin Air Force Base, USA, under the auspices of TTCP WTP-3. The components form a simpler three-detector VISAR rather than the more recent and sophisticated four-detector version [6]. The system developed around these components includes a high-power laser, electro-optic shutter, and a computer-based data acquisition, processing and data reduction facility. We have reached a stage where data can be obtained for small- and medium-scale flyers (0.25 mm and 1.5 mm bridge widths, respectively). Its application to large-scale flyers has not been evaluated and attempts at free-surface velocity measurements have not been conclusive.

The present report provides details on the VISAR system, some results, and discusses the system's limitations as shown by these results.

2. Three-Detector VISAR System

2.1 Principle of Operation

2.1.1 General Description

A VISAR measures velocities by using the Doppler shift of a laser beam diffusely reflected from a moving target (Fig. 1). The VISAR optics and detector parts were made by Systems, Science and Software (Model 3SLVI-401), with the remaining parts being added by MRL. During a measurement, an electro-optic shutter allows a high powered argon-ion laser beam to pass through the hole in mirror *M*. The beam is then focused on to the target by lens *L*. The diffusely reflected beam is collected and recollimated by *L*, after which it is reflected by *M* and enters the VISAR optics.

After *M*, the beam passes through a beam reducing telescope, followed by a polarizer set to give a linearly polarized beam with its plane of vibration about 45° to the vertical. The monitor beamsplitter (MBS) then directs a fraction of the beam to the monitor photomultiplier. The recording of beam intensity during the measurement is needed for the correction of intensity variations and for subtracting incoherent light information from the data signals.

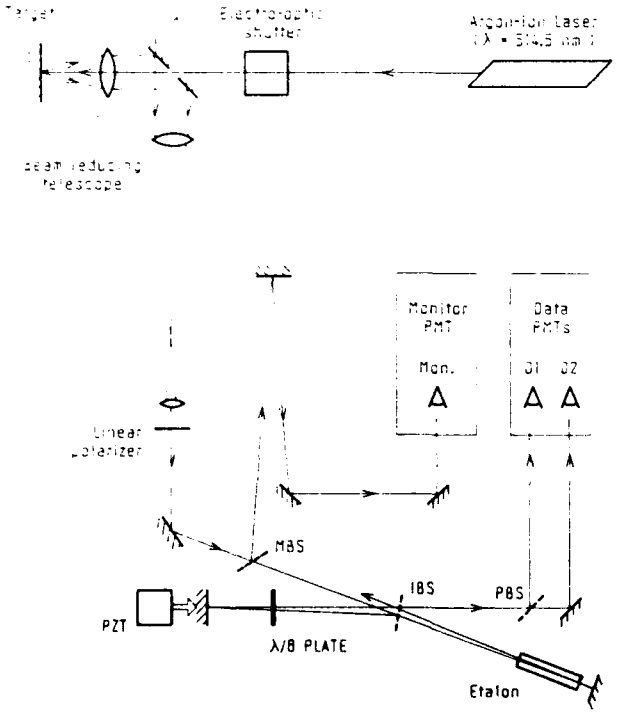

Figure 1: *VISAR schematic diagram.*

The transmitted fraction of the beam enters the modified Michelson-type interferometer where it is first split into equal parts by the interference beamsplitter (IBS). The interferometer is set up so that the apparent optical path lengths of the two arms are equal to allow interference of spatially incoherent light, but at the same time with light from one arm delayed in time so that fringe shifts occur with wavelength changes. Both of these requirements are satisfied by the use of a solid etalon in one arm. The light reflected along the non-delay arm passes twice through an eighth retardation plate thereby converting the linear polarization to circular polarization. This allows quadrature coding of the signals which is used to improve the resolution of the system near maximum or minimum of the fringes. It also allows the sign of the acceleration to be determined without ambiguity [1].

Upon recombination at the IBS, the beams undergo interference. One recombined beam is directed via a polarizing beamsplitter cube (PBS) and mirror to the data photomultipliers, while the other recombined beam is wasted. The PBS resolves the beam into its *s* (vertical) and *p* (horizontal) components which are detected by the D1 and D2 photomultipliers respectively.

As shown in the instrumentation schematic in Figure 2, the three photomultiplier outputs are recorded by a digital storage oscilloscope (DSO). A delay pulse generator provides the required triggering sequence for the electro-optic shutter, photomultipliers, firing equipment, and oscilloscope.

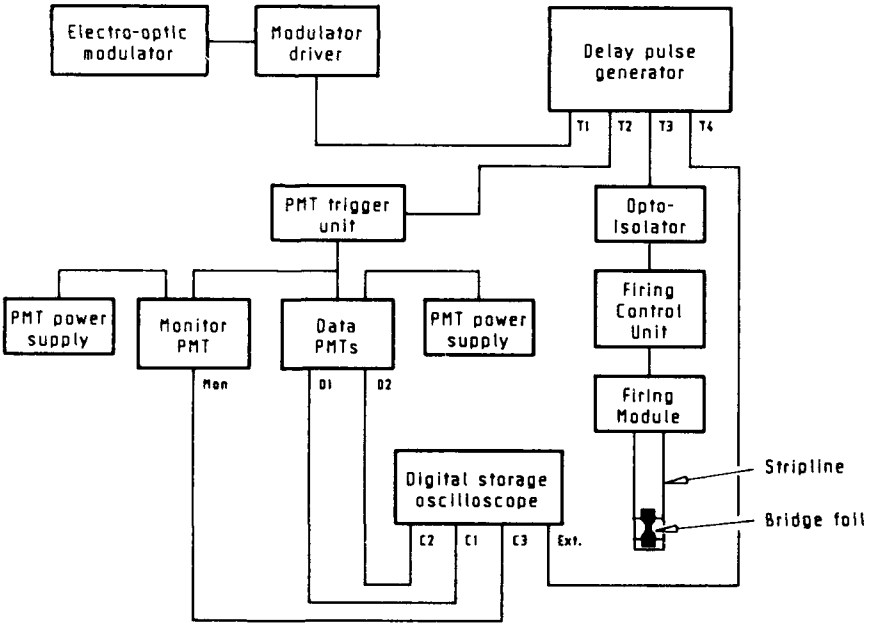

Figure 2: Block diagram of the instrumentation arrangement.

2.1.2 *VISAR Equations*

Velocity

The expression usually used for calculating the velocity, $u(t)$, at time t is as follows [6]:

$$u(t) = \frac{\lambda_0 c F(t)}{4 l_e (n_e - 1/n_e)(1 + \delta)} \tag{1}$$

where

λ_0	=	wavelength of the unshifted light,
c	=	speed of light,
$F(t)$	=	total fringe count at time t,
l_e	=	length of etalon,
n_e	=	refractive index of the etalon material, and
δ	=	correction for the optical dispersion of the etalon.

Another commonly used expression is the velocity fringe constant, K, where

$$K = \frac{\lambda_0 c}{4 l_e (n_e - 1/n_e)(1 + \delta)} \tag{2}$$

Various derivations of the velocity interferometer equation are given in the literature [7, 8, 9, 10]. An alternative derivation is given in Appendix A. The equation includes an additional term which accounts for the effective etalon length of the $\lambda/8$ waveplate/IBS combination.

Translation of the Delay-Arm Mirror

As mentioned above, the etalon is used both to allow interference of spatially incoherent light and to introduce a time delay. After an etalon of length l_e is inserted, the mirror in the delay arm must be moved by an amount x. As shown in Appendix B, x is determined by the expression

$$x = l_e\left(1 - \frac{1}{n_e}\right) \tag{3}$$

where

n_e	=	the refractive index of the etalon material
	=	1.462 for fused silica at λ = 514.5 nm.

Translation of the mirror by x ensures that split rays of spatially incoherent light will be recombined with themselves at the IBS. While spatial incoherence is not required in this arrangement, temporal coherence is, as the optical path difference is significantly greater than zero.

2.2 *Laser*

For this work, a Coherent Innova 90-5 5-watt argon-ion laser is used in the single line mode. The chosen line of 514.5 nm, selected by means of an air-spaced etalon and a single line prism, has a maximum output power of approximately 1 watt.

2.3 *Electro-Optic Shutter*

Since the laser beam can be focused to a high power density, an electro-optic shutter is used to control the time the target is exposed to the beam, thereby minimizing thermal damage effects. As shown in Figure 3, the electro-optic shutter comprises an electro-optic modulator (Inrad Model 101-020) and a prism polarizer (Inrad Model 701-050). The modulator is a single crystal KD*P modulator with a half-wave voltage of about 3 kV at λ = 514.5 nm. The prism polarizer is of the Glan-Foucault type and is constructed from calcite.

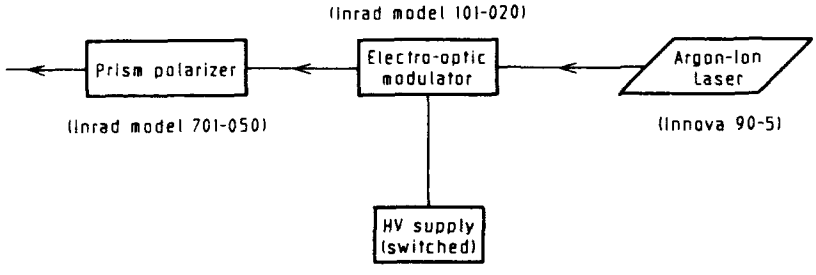

Figure 3: Block diagram of the electro-optic shutter arrangement.

During operation, the nominal 3 kV is applied to the modulator causing the vertical linearly polarized light from the laser to be rotated through 90° and thus reflected by the polarizer. Switching the applied voltage to essentially zero volts just prior to firing of an exploding bridge foil flyer generator allows the laser beam to pass through the polarizer to the target for a duration of about 10 ms. The high voltage is switched by SCRs in a unit made at MRL. The rise time of the shutter is less than 2 μs.

2.4 *PMT Arrangements*

As shown in the circuit schematic of Figure 4, the photomultipliers (RCA 7326) are used in pulsed mode. Pulsed mode enables large tube currents to be drawn so that useful signals can be achieved across a 50 ohm load impedance. It also reduces the chance of the PMTs being inadvertently exposed to large ambient light levels. Triggering is by means of a capacitor discharge ($\tau \approx 0.2$ ms) provided by a PMT Trigger Unit (Fig. 5). For operating a piezoelectric translator (see Section 2.6.2), the unit also provides switch-selectable Pulse, AC or DC voltages.

The data PMTs have a common HV power supply but separate voltage divider networks. The three PMTs are operated at the manufacturer's recommended maximum operating voltage of - 2.4 kV. As is the recommended practice for PMTs operated in pulsed mode [12], the last stages have relatively large bypass capacitors to provide improved linearity of the tubes. As a simple check for tube linearity, an incandescent globe was operated at a fixed voltage and distance from a PMT. Intensity variations were produced by placing neutral density filters between the PMT and the globe (laser line filter being removed). No significant departures from linearity were observed for PMT output voltages up to about 0.75 V (Fig. 6).

The PMTs have nominal pulse risetimes of 2.8 ns. Thus, to ensure high frequency response, the PMTs are connected to the DSOs by 50 ohm (RG58/U) coaxial cables and in the event that the DSOs do not have 50 ohm input impedance, a 50 ohm in-line cable terminator is used. For correct synchronization of signals, the cable lengths are matched so that transit times are within 1 ns of each other. When the PMTs are triggered a dark current pulse is observed. Synchronization of an event is arranged so that the data signals occur after this pulse; a delay of a few μs is required.

Diffusers, laser line filters (3 nm FWHM), and iris diaphragms are used in front of each PMT (Fig. 7). The diffuser distributes the incoming light over the photocathode surface to mitigate the effect of motion of the light [13]. The filters also offer protection to PMTs used under ambient light conditions but, more importantly, prevent much of the light from the self-luminous target from reaching the PMTs. The diaphragms facilitate aperture selection.

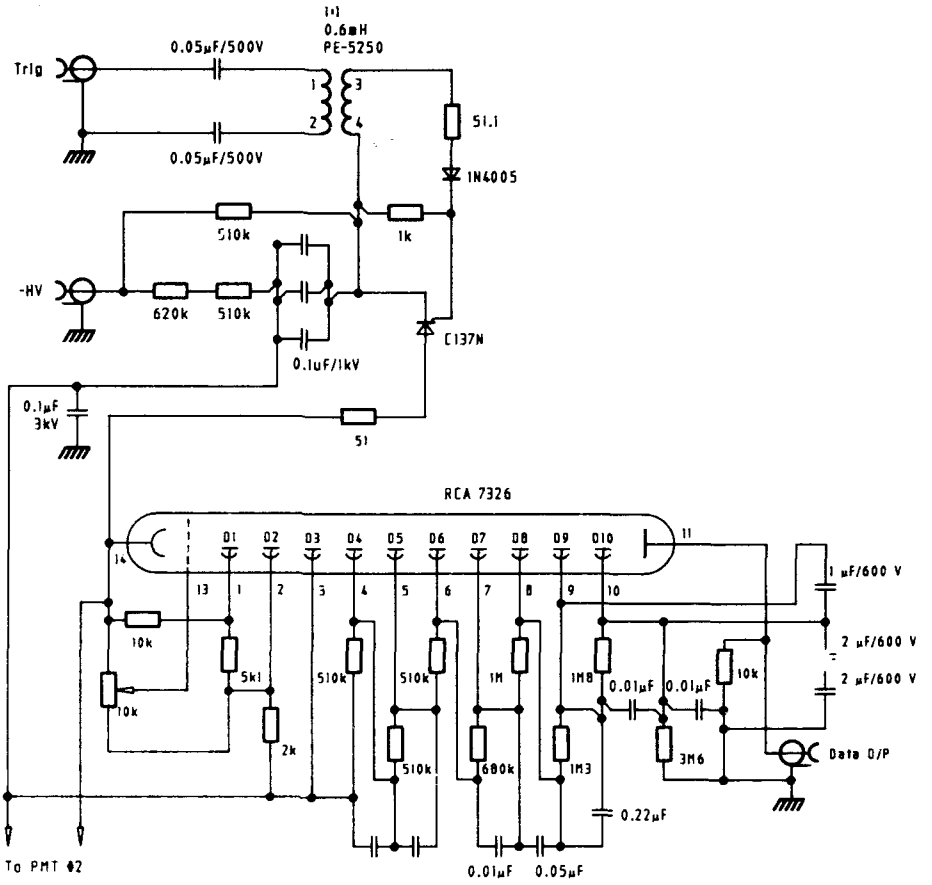

Figure 4: S^3 VISAR Model 3SLVI-401 photomultiplier arrangement.

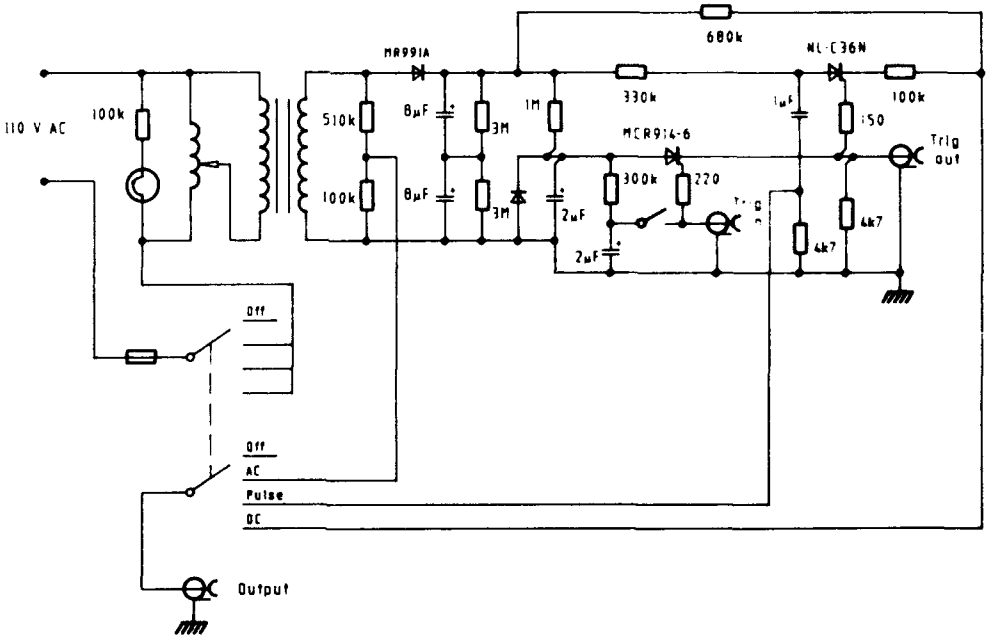

Figure 5: S^3 VISAR Model 3SLVI-401 photomultiplier trigger unit arrangement.

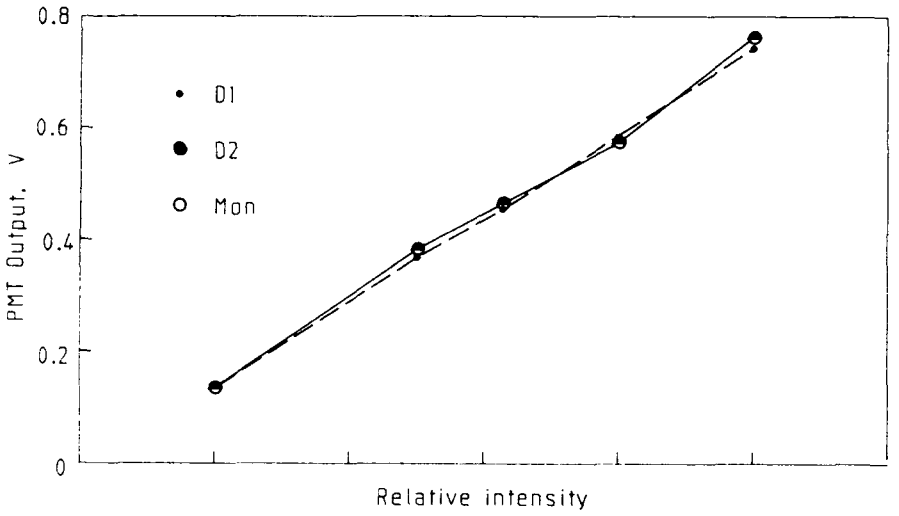

Figure 6: Photomultiplier linearity data.

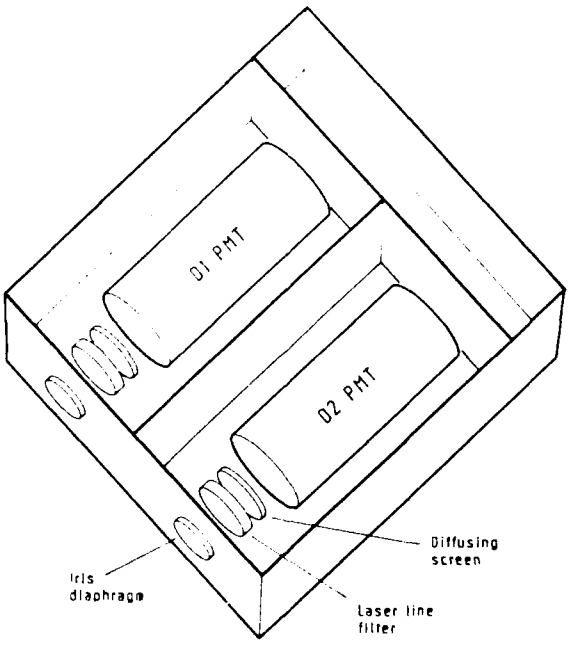

Figure 7: Photomultiplier housing.

2.5 *Target Alignment*

Various lenses were available for use as the target lens (Table 1). The lens focal length and its distance from the VISAR optics determines the rate of change of intensity of the return beam with target motion. As shown in Appendix C, the intensity I after travel of Δx is given by

$$I = \frac{I_0}{(1 + S\Delta x/f^2)^2} \tag{4}$$

where

I_0 = initial intensity,
S = lens to VISAR optics distance, and
f = focal length.

Table 1: Lens Characteristics

Form	Focal Length (mm)	Aperture Diameter (mm)	F/#
Biconvex	189.0	41.5	4.6
Achromat	79.0	32.0	2.5
Plano-convex	50.2	32.0	1.6

This expression implies that it would be best to have a long focal length lens, close to the VISAR table. However, in practice this is not the case for EBF generators which are strong sources of electromagnetic interference (EMI). As EMI can have adverse effects on the quality of the PMT signals, large S can be beneficial. Distance also helps to prevent incoherent light from entering the VISAR. Focal length and aperture together determine the efficiency of the lens for collecting the diffusely reflected light; thus a large diameter lens of short focal length would be best. A short focal length lens also produces a beam of finer speckle. The effects of speckle are uncertain; its motion can affect fringe quality [6].

The above two effects cause some conflict when choosing a lens. Through experience, the plano-convex lens of focal length 50.2 mm has been preferred. By calculation, the diffraction limited spot diameter on the target would be about 10 μm. Observation through a microscope shows the diameter to be less than 50 μm [15]. In choosing a lens, consideration should also be given to the space needed between the lens and target to mount a protective glass barrier and for the insertion of alignment aids (discussed below).

2.6 *Interferometer Adjustments*

2.6.1 *Alignment*

(i) The electro-optic modulator and prism polarizer are set up with their optic axes coincident with the laser beam axis. To avoid the possibility of mode-pulling, they are then tilted slightly to ensure surface reflections are not returned directly into the laser. The laser beam (approximately 2 mm diameter) is then directed centrally through the 5 mm diameter aperture in the large turning mirror.

(ii) Diffuse reflection from a plaster target is recollimated by the target lens. Collimation is checked by moving between the lens and the turning mirror an index card with a 2 mm diameter aperture.

(iii) The optic axis of the target lens is set coincident with the laser beam axis. For this adjustment, the index card is placed just in front of the turning mirror. The lens position is then adjusted until the centre of the recollimated beam is coincident with the centre of the card aperture. The lens is then rotated about the vertical or horizontal axis slightly to prevent surface reflections returning to the laser and the VISAR optics.

(iv) The large turning mirror is removed and replaced by a smaller mirror set to turn the laser beam through 45° to enter the beam reducing telescope. The index card mentioned above is placed just before this mirror. By observing reflections from the front and rear surfaces of the telescope lenses, the mirror is adjusted until the beam passes centrally through both lenses. The distance between the lenses is changed by moving the smaller lens until the reduced beam is slightly divergent through the rest of the optics. Ideally, the adjustment would be such that the reduced beam was well collimated but lens aberrations prevent this.

(v) The polarizer is positioned so that the beam passes centrally through it.

(vi) The mirror following the telescope is adjusted to direct the beam along the optic axis of the etalon which is held in a vee block.

(vii) The mirror in the delay arm is moved to approximately the equi-arm position and tilted until the beam reflected on return to the IBS is centred on the PBS. The PBS and the following mirror may then need to be tilted until the beams are centred on the data PMT apertures.

(viii) The monitor beam, reflected by the MBS, is also centred on the MON PMT aperture. In order to obtain equal solid angles [13] and for synchronization purposes [1], the path lengths from the MBS to the MON, D1, and D2 PMTs must be the same.

(ix) Divergence of the laser beam causes the beam diameter at the PMTs to be about 10 mm, which is too large for accurate centering on the PMT apertures. Therefore, a 300 mm focal length biconvex lens is installed temporarily just before the MBS to focus the beam to a 2 mm diameter at

the apertures. The centering of the lens with the beam is again ascertained by viewing reflections from front and back surfaces. With the PMT apertures set to 2 mm diameter, minor adjustments of mirrors are made until the beam axes are coincident with the centre of the apertures.

(x) The 300 mm focal length lens is removed and the mirror in the non-delay arm adjusted until fringes appear on a white index card placed in front of the PMTs.

(xi) For the next procedure, the laser beam is not used. Instead, a low pressure Hg-vapour lamp is placed just before the IBS. This lamp has a shorter coherence length than the laser beam and is used to obtain an initial position for the delay mirror for the interferometer without an etalon. The delay arm mirror is moved until the fringes appear to have the best visibility. This position is not clearly defined but gives a satisfactory starting point for obtaining fringes when the lamp is replaced with an incandescent source (12 V/60 W globe); fringes are again found by moving the mirror slowly over a short range about this point. This operation needs to be performed with some finesse as the fringes only appear over a range of about 25 μm (50 λ). This then gives the required delay mirror position before additional etalons are inserted to obtain the required fringe constant.

(xii) After an etalon is inserted, the delay mirror must be translated. The arms of the interferometer are not quite compensated since the IBS and λ/8 waveplate optical path lengths are not the same (different thicknesses and refractive indices). The amount of translation must be adjusted accordingly (Appendix A). During translation, slight loss of alignment may occur but is easily restored by slight adjustment of the delay mirror (rather than the fixed mirror which might result in loss of coincidence with the monitor).

(xiii) The large turning mirror is re-installed and, if necessary, adjusted until the reflected beam from the plaster target is centred on the PMT apertures.

2.6.2 *Lissajous Figures*

Lissajous figures (X-Y plots) obtained from the D1 and D2 signals play an important role in the VISAR system. They are used:

(i) as an aid in setting up the interferometer optics.

(ii) as a diagnostic tool for indicating the quality of the data. Ideally, the Lissajous figure would be a series of nearly concentric circles with nearly equal radii. Any imperfections in the system result in non-ideal figures.

(iii) when adjusting the data before a velocity calculation is performed.

The first use is described below. The other two uses are addressed in later sections.

By suitable adjustment of the linear polarizer and the $\lambda/8$ waveplate, the D1 and D2 PMT signal amplitudes can be made equal and 90° out of phase. With the polarizer initially set to about 45° to the vertical, the non-delay arm is blocked by a card so that only the delay arm beam passes through to the data PMTs. Continuing to use the plaster target, the laser power is increased to greater than 0.5 W, after which the PMTs are triggered and their outputs recorded by the DSO. The two traces should be of equal amplitude; if not, the polarizer is rotated until they are. The above is repeated with the delay arm blocked but to obtain equal amplitude traces the $\lambda/8$ waveplate is rotated instead. The card is removed so that fringes are again formed.

The non-delay arm mirror has been mounted to a piezoelectric translator (PZT) which is used to quickly move the mirror, thereby causing the fringes to shift. These fringes are recorded by the DSO (Fig. 8). With the DSO configured for X-Y operation, the trace (Lissajous figure) should be a circle (Fig. 9). If the figure is elliptical, the polarizer and/or $\lambda/8$ waveplate will need some slight readjustment.

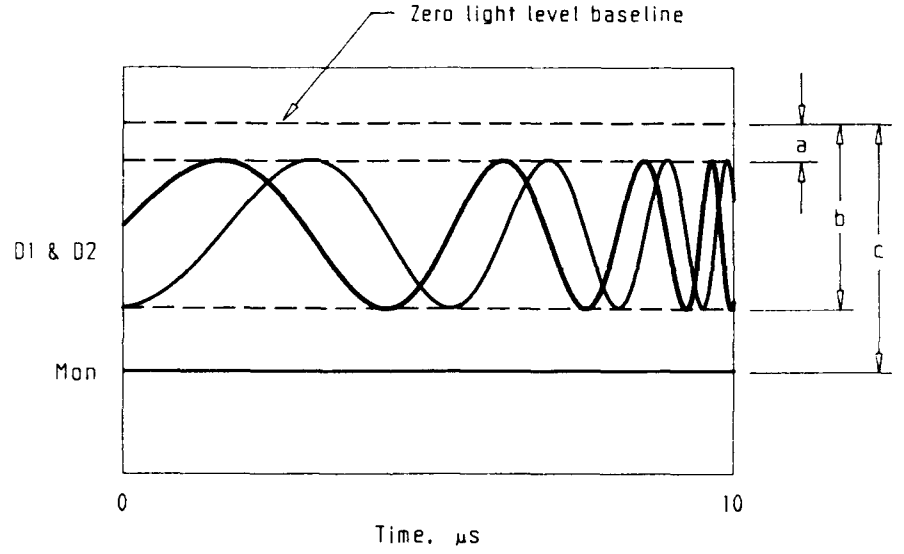

Figure 8: *Form of test fringes generated by displacement of the mirror in the non-delay arm by the PZT. Typical values for a, b, and c are 10 mV, 200 mV, and 250 mV respectively.*

2.6.3 *Beam Intensity Factor*

As discussed in Appendix D, the monitor PMT signal needs to be scaled before use in adjusting the data PMT signals. In order to determine the scaling factor, γ, operation of the PZT is again used to produce fringes but this time all three PMT signals are recorded. Using the parameters shown in Figure 8, the scaling factor is calculated as follows:

$$\text{Beam Intensity Factor} = \gamma = \frac{a+b}{2c} \qquad (5)$$

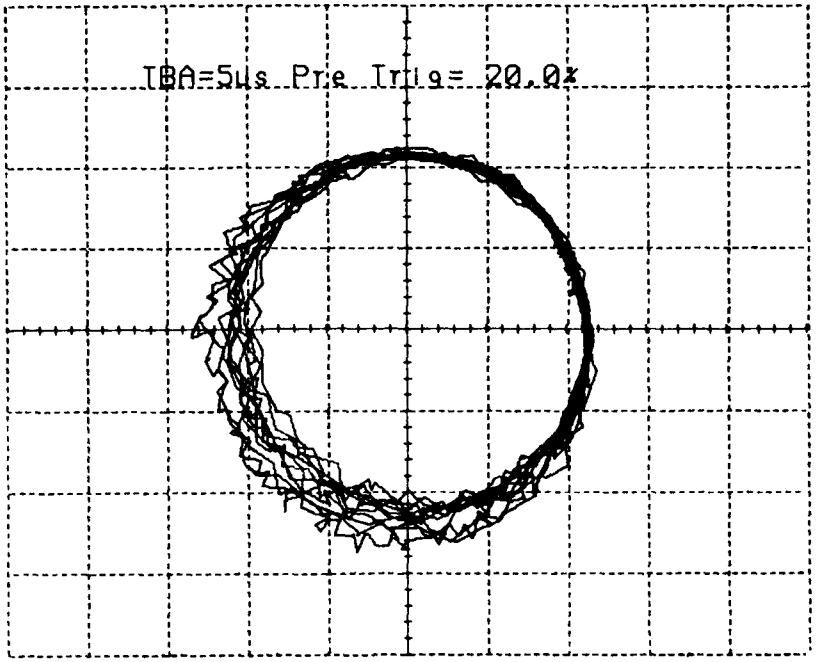

Figure 9: Circular Lissajous figure produced from the test fringes.

3. Data Manipulation

3.1 Post Processing

To enable reduction to a velocity-time history, the data recorded by the oscilloscope are transferred by means of a GPIB (IEEE-488) communications channel to an IBM PC/AT compatible computer. A scientific software package, Asystant GPIB, is used to effect this transfer. A series of Asystant routines then scale the monitor signal, the scaled signal in turn being used to correct the data signals. Should the record lengths be too long, the routines can be used to remove the unwanted data. The corrected data are then displayed in Y-t and X-Y formats. The last operation to be performed under Asystant is to convert the data stored in Asystant files to ASCII files suitable for a second data reduction program.

3.2 *Data Reduction*

The second program was written in Pascal several years ago prior to the commissioning of the VISAR. Unfortunately, at the time it was necessary to postpone the incorporation of the data transfer and correction process now done using Asystant. The Pascal program thus requires "well-behaved" data, i.e. sine- and cosine-type signals. There is no provision in the program for the removal of signal imperfections caused by beam intensity variations and incoherent light. It has various option menus for data processing but the main one used is interactive centering of the Lissajous figure (for final adjustment of the offset). The other options include adjustments for polarization and time synchronization problems, and the elimination of bad data points. If required, a data smoothing routine can be invoked. Once the Lissajous figure is centered to the operator's satisfaction, the velocity-time history is calculated using an arctangent algorithm [14].

4. *VISAR Tests*

4.1 *Tests Conducted*

For the process of characterizing and optimizing the VISAR for flyer studies, a medium-scale exploding bridge foil flyer generator (Fig. 10) and flyer thicknesses of 25 μm and 50 μm were used. Being able to readily align the 1.5 mm wide bridge foil with the laser beam by eye was the main reason for selecting this generator. In addition, the firing equipment used for these EBF flyer generators was suitable for many repeat firings. Many investigative firings were required before repeatable and sensible data for these flyers ensued, which in turn enabled tests with small flyers to proceed.

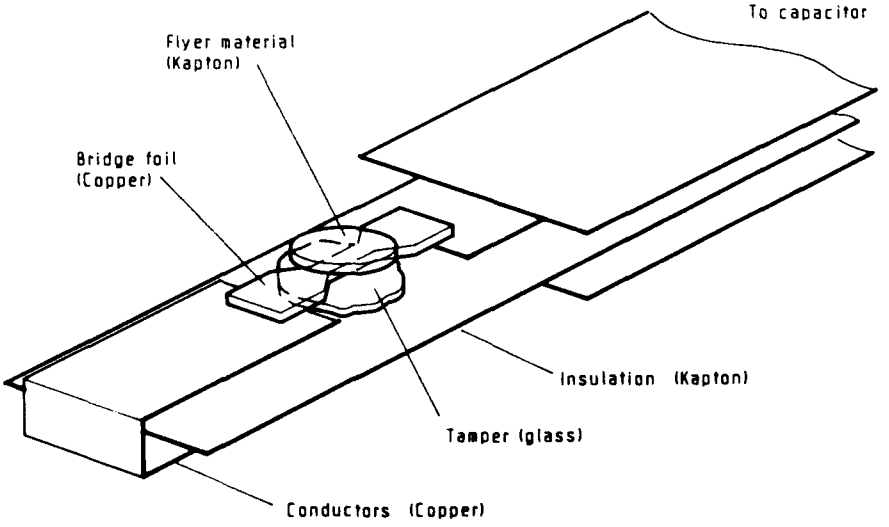

***Figure 10:** Exploding bridge foil (EBF) flyer generator.*

For an initial assessment of the suitability of the VISAR for small-scale flyers (0.25 mm bridge width), some firings were made using the medium-scale flyer set-up. Even though the inductance of the firing equipment/stripline combination is significantly greater than that used in practice for small flyers, similar peak velocities can be obtained. Later, tests were conducted using a low inductance assembly after it was found that an experimental integral stripline switch [15] enabled repeat firings to be easily conducted.

Another application of interest for the VISAR is free-surface velocity measurements which enable Hugoniot data to be obtained for materials subjected to shock stresses. An assessment of the suitability of the VISAR for these measurements was also made.

For all of the above measurements, the frequency response of the PMTs needs to be high. In relation to this requirement, the response of the PMTs to a short duration light pulse (simulated delta function pulse) was examined.

The fringe constants and corresponding etalon lengths used for the tests are given in Table 2.

Table 2: Etalon Lengths and Fringe Constants

Etalon Length (mm)	Fringe Constant (m/s)
49.74	964
24.77	1937
17.91	2678
12.45	3853

Note: The fringe constant was calculated using equation (1) because the interferometer was erroneously set up in that the delay mirror translation did not include Δl (equation (5), Appendix A).

4.2 *Firing Equipment*

The firing equipment for the medium-scale flyer tests comprised a Reynolds FS-14 control unit and a customized firing module. The 0.2 μF capacitor in the module is a low inductance type with a configuration suitable for connection to a stripline. The circuit inductance and resistance of the capacitor/stripline assembly was typically 60 nH and 0.1 ohm, respectively.

The HV power supply in an MRL constructed firing equipment for use with low inductance capacitor/stripline assemblies operates in a simple transformer mode using a quadrupler [16]. The equipment comprises the HV supply and a trigger unit [15]. The maximum output is about 2 kV, with the adjustable amplitude trigger pulse being used to operate the stripline switch. When using a 0.2 μF firing capacitor (Custom KM 36), the circuit inductance and resistance for the capacitor/stripline assembly was typically 13 nH and 0.12 ohm, respectively.

To reduce EMI noise effects on the photomultipliers, the firing equipment and test assemblies were housed in a double electrically isolated Faraday enclosure.

4.3 *Treatment of the Flyer Surface*

Treatment of the flyer surface in order to obtain diffuse reflection is of paramount importance for the collection of good VISAR data. Should the reflection be too specular, the measurement fails through gross beam intensity changes. Even with adequate treatment of the surface, significant beam intensity variations occur as shown by the monitor signal in Figure 11. This profile is considered to be a result of a number of effects:

1. self-light produced at bridge burst (Fig. 12);
2. change in reflectivity due to shock induced change in the refractive index of the flyer;
3. convexity of the surface prior to flyer formation;
4. changes in tilt of the flyer; and
5. changes in collimation of the return beam due to flyer motion.

Various forms of treatment were considered. Placing a small piece of black "letraset" over the flyer was one of the initial treatments used and this was fairly successful. Unfortunately, the added mass of the "letraset" is significant compared to that of the flyer itself. Working the surface with emery polishing paper (grade 3/0) occasionally produced reasonable data. Chemical etching and coating by sputtering techniques were contemplated but none were tried. Though considered at the outset, grit blasting of the surface was not tried until equipment related delays had been overcome. This treatment gives good results and is the one favoured by many other laboratories.

A number of grit blasting techniques were tried. Initially, it was found that by operating a large-scale machine (Cyclo-blast, Model 14689) at low pressure (≈ 25 kPa) reasonable surface finishes could be obtained on most occasions. This machine is normally loaded with about 250 μm grit, which would be unsuitable at normal pressures. But it is believed that operation at low pressure results in smaller grit being selected. However, there is an undesirable lack of control over grit size, which means the treatment is not always reproducible. Much more satisfactory results were obtained by grit blasting the flyer surface for about 10 seconds using a miniature grit-blaster (Paasche Airbrush Co., Model AECR-879) at a canister pressure of 180 kPa. The abrasive compound used in the blaster was domestic grade sodium bicarbonate. Examination of the surfaces under a microscope showed that the peak-to-valley distances were less for the miniature blaster compared to the large machine.

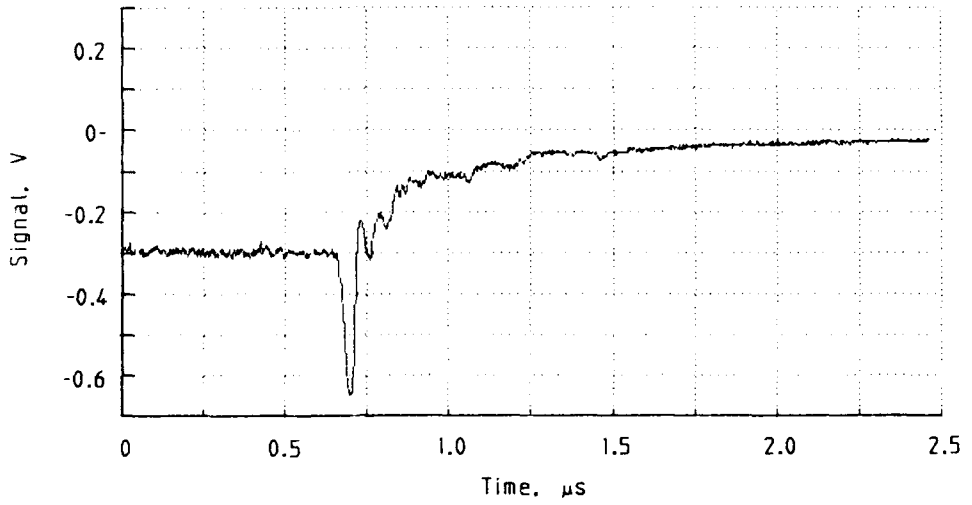

Figure 11: Monitor photomultiplier signal showing rapid intensity changes during an EBF flyer generator firing (25 μm flyer thickness, 1.5 mm bridge foil width, 5.4 kV).

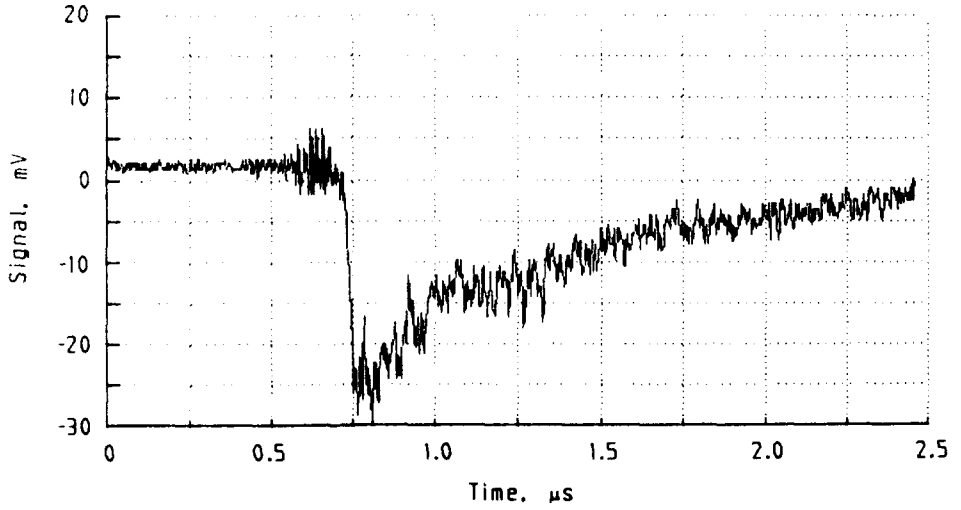

Figure 12: Monitor photomultiplier signal showing self-light produced by a bridge foil burst (25 μm flyer thickness, 1.5 mm bridge foil width).

4.4 *Laser Beam/Bridge Foil Alignment*

As mentioned above, the laser beam was centered on the bridge foil. For the medium-scale flyers this was performed with the unaided eye but was done with the assistance of a 4X jeweller's eyepiece for the small-scale bridge foils. In both cases low beam intensity was used; this was achieved by operating the Pockels cell with the laser at its lowest power setting (2 mW).

4.5 *EBF Generator Preparation*

After grit blasting, a glass tamper was attached to the bridge foil using cyanoacrylate adhesive. The medium-scale bridges were then attached to the striplines using masking tape. An additional step was introduced for the small-scale generators whereby the tamper was first viewed under a microscope in order to examine in general the integrity of the bond, but in particular that the interface between the foil and glass was free of air bubbles. While under the microscope the flyer surface was inspected for grit and scratches. Bridges free of tamper and surface faults were then attached to the striplines by soldering.

4.6 *Free-Surface Velocity Measurements*

The experimental arrangement used for performing these measurements is shown in Figure 13. The impact side of the polycarbonate target was sprayed with a thin coat of black paint to block reflections from surfaces other than the surface of interest. The thickness of the polycarbonate targets ranged from 0.15 mm to 1.05 mm. The medium-scale EBF flyer generator was operated at a firing voltage of 5.4 kV to produce a flyer with a velocity of about 2450 m/s, as shown below. The free-surface velocity would be about the same as the flyer velocity when several conditions are met: the impact is symmetric, the shock pressure is less than 50 GPa [17], and the target is thin (shock pressure not attenuated by release waves); on this basis the maximum free-surface velocity that could be attained would be about 2450 m/s.

4.7 *PMT Anode Pulse Rise Time Measurement*

For examining the anode pulse rise time of the PMTs, an optical pulser comprising a transistor operated in an avalanche mode and a sub-miniature red LED was constructed (Fig. 14). The light from the LED was coupled directly to the PMT photocathode by a fibre-optic cable. The rise time of the avalanche current pulse through the LED (Fig. 15) was slightly less than 1 ns. The duration of the pulse was adjusted by the length of the RG58 coaxial cable charge line. The shortest duration (≈ 5 ns) was obtained when the charge line was removed altogether, stray capacitance being found sufficient for operation of the LED.

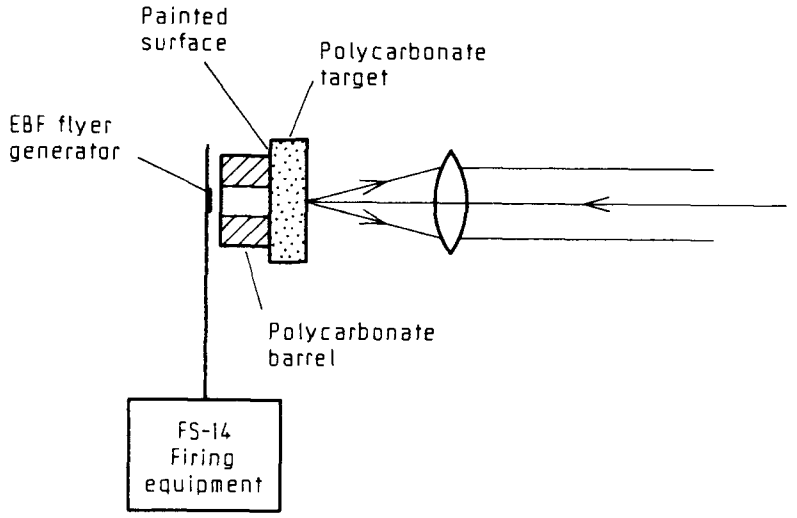

Figure 13: Arrangement for free-surface velocity measurements.

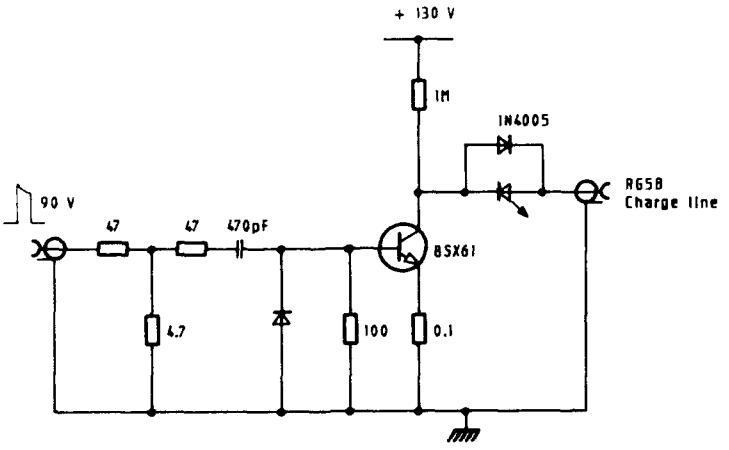

Figure 14: Optical pulser circuit schematic.

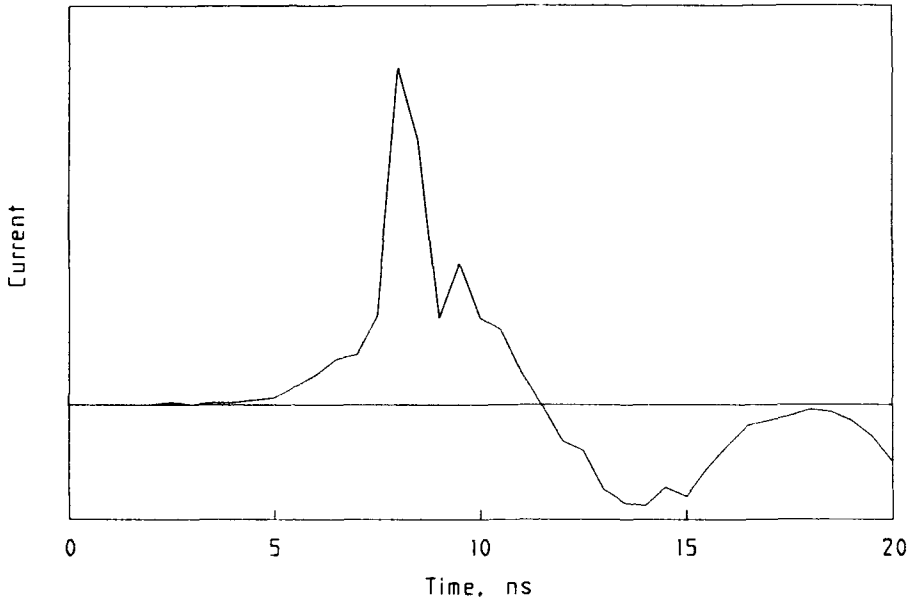

Figure 15: LED drive current pulse.

5. Results

5.1 Medium-Scale Flyers

Firings were conducted at a firing capacitor charge voltage of 5.4 kV, with a fringe constant of 964 m/s. The flyer surfaces were prepared using the large-scale grit blasting machine. For the 25 μm thick flyers, a Lissajous figure and data signals from one of the firings are shown in Figures 16 and 17 respectively. For the other firings, the spiralling collapse of the Lissajous figures was a little greater. Velocity-time histories from three repeat firings are shown in Figure 18. The peak velocities were about 2450 m/s, the peak accelerations about 20 Gm/s^2, and the flyers travelled about 1 mm before their peak velocities were reached.

For a 50 μm thick flyer, a Lissajous figure and data signals are shown in Figures 19 and 20 respectively. Velocity-time histories for three repeat firings are shown in Figure 21. The peak velocities were about 1500 m/s, the peak accelerations about 10 Gm/s^2, and again the flyers had travelled about 1 mm before reaching their peak velocities.

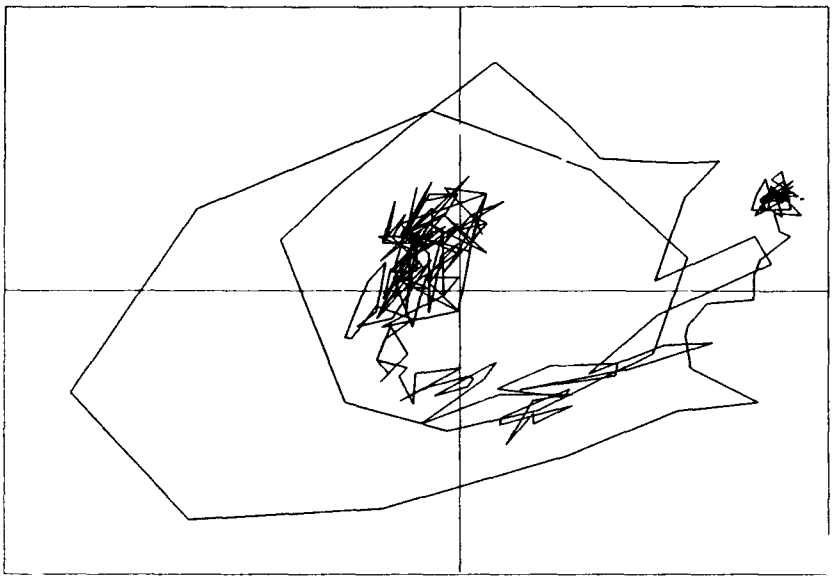

Figure 16: Lissajous figure (25 μm flyer thickness, 1.5 mm bridge width, 5.4 kV).

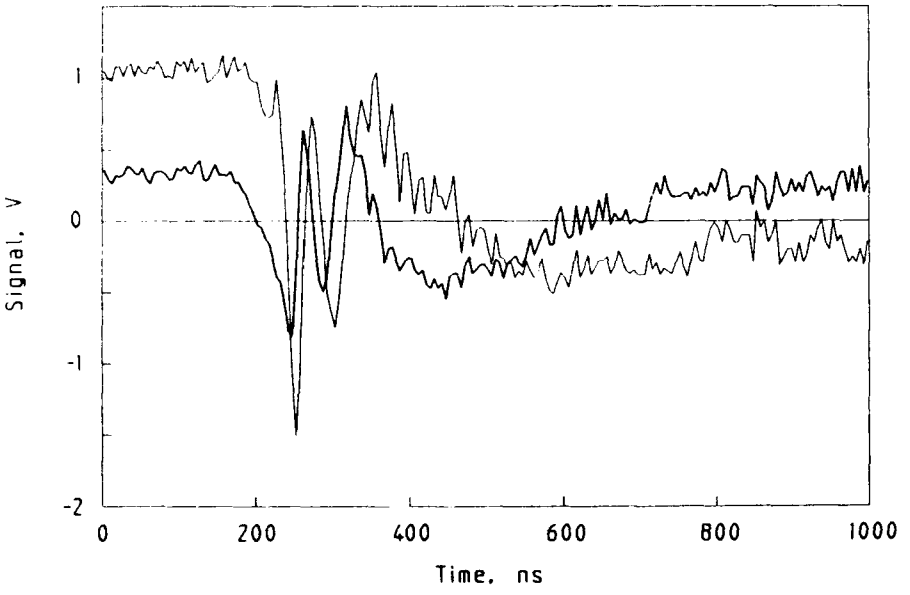

Figure 17: Corrected VISAR data signals (25 μm flyer thickness, 1.5 mm bridge width, 5.4 kV).

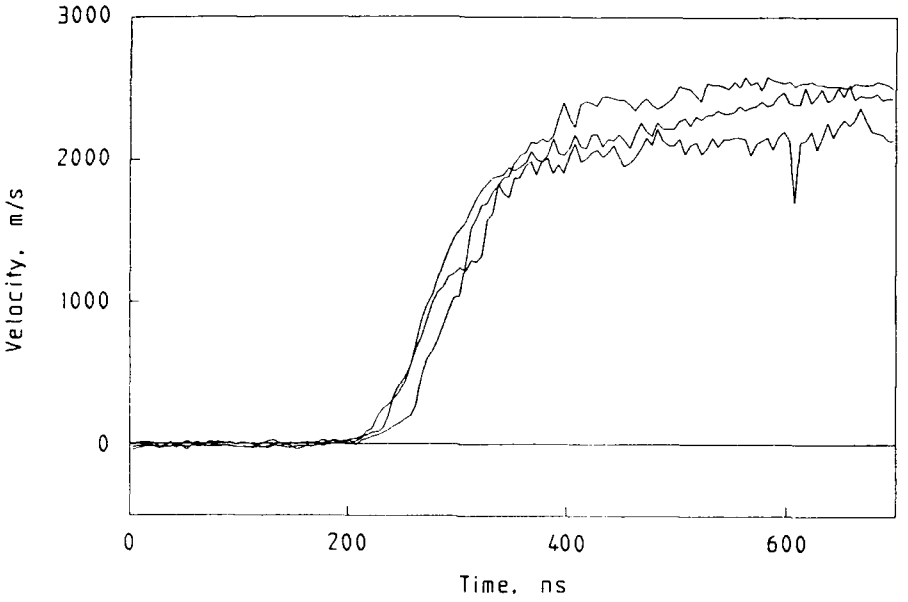

Figure 18: Velocity-time histories (25 μm flyer thickness, 1.5 mm bridge width, 5.4 kV).

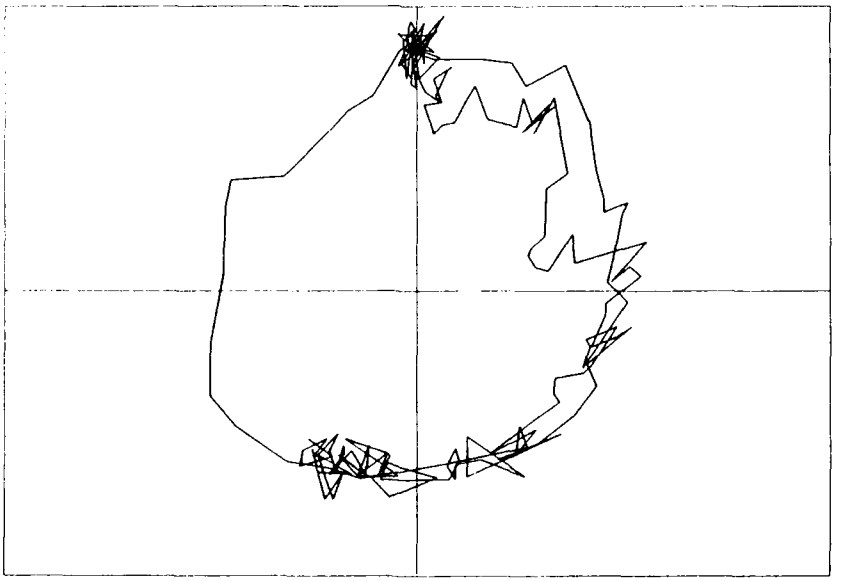

Figure 19: Lissajous figure (50 μm flyer thickness, 1.5 mm bridge width, 5.4 kV).

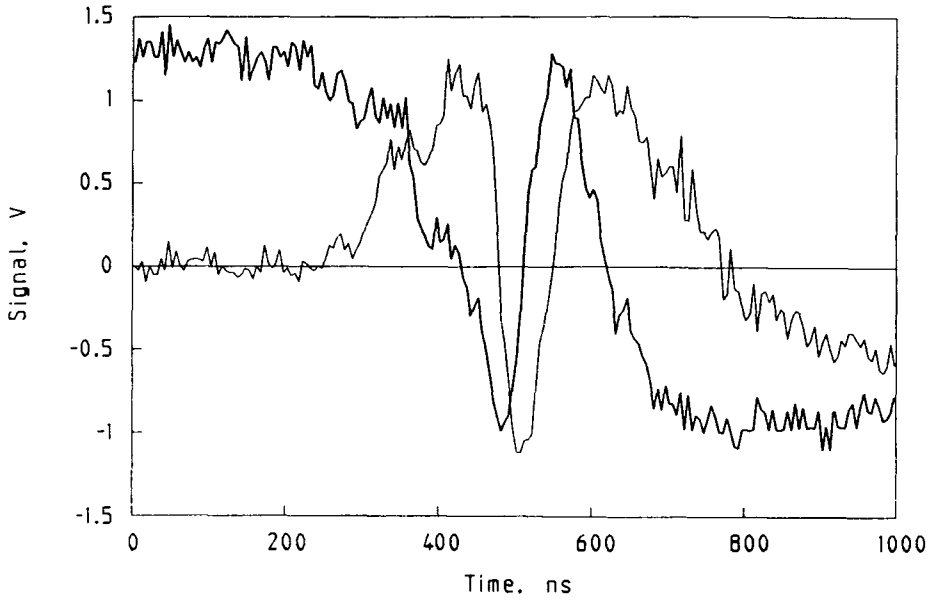

Figure 20: Corrected VISAR data signals (50 μm flyer thickness, 1.5 mm bridge width, 5.4 kV).

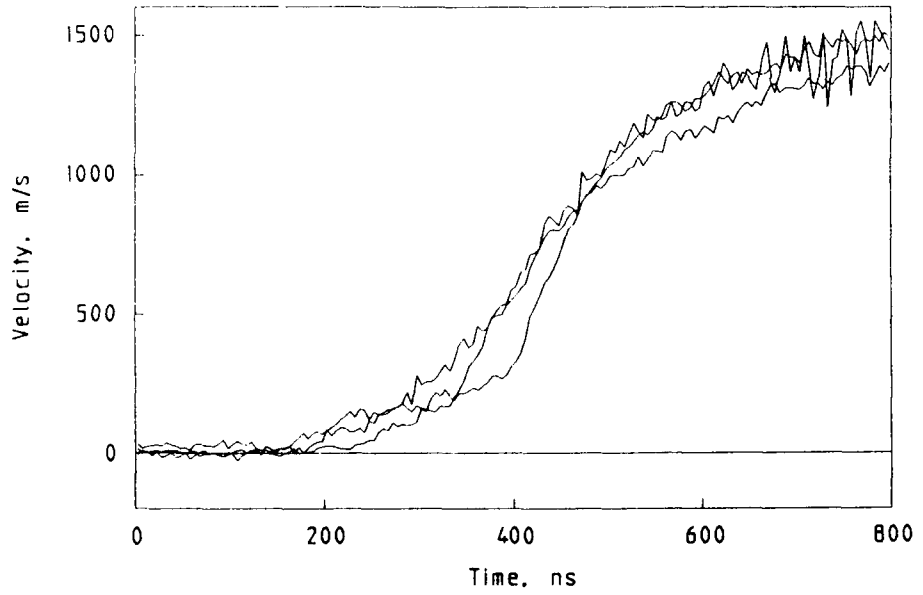

Figure 21: Velocity-time histories (50 μm flyer thickness, 1.5 mm bridge width, 5.4 kV).

5.2 Small-Scale Flyers

5.2.1 FS-14 Firing Equipment

Firings at 2.0 kV with the same fringe constant, 964 m/s, and surface treatment used for the medium-scale flyers produced poor quality data. Rapid spiralling collapse of the Lissajous figures occurred, with signs of fringes being lost. But by doubling the firing constant to 1937 m/s, the Lissajous figures were similar to those obtained for the medium-scale flyers. Velocity-time histories for three repeat firings are shown in Figure 22. The peak velocities were about 3200 m/s, the peak accelerations about 50 Gm/s^2, and the peak velocities were reached after the flyers had travelled about 0.25 mm. A firing at 3.0 kV produced a peak velocity of at least 5000 m/s.

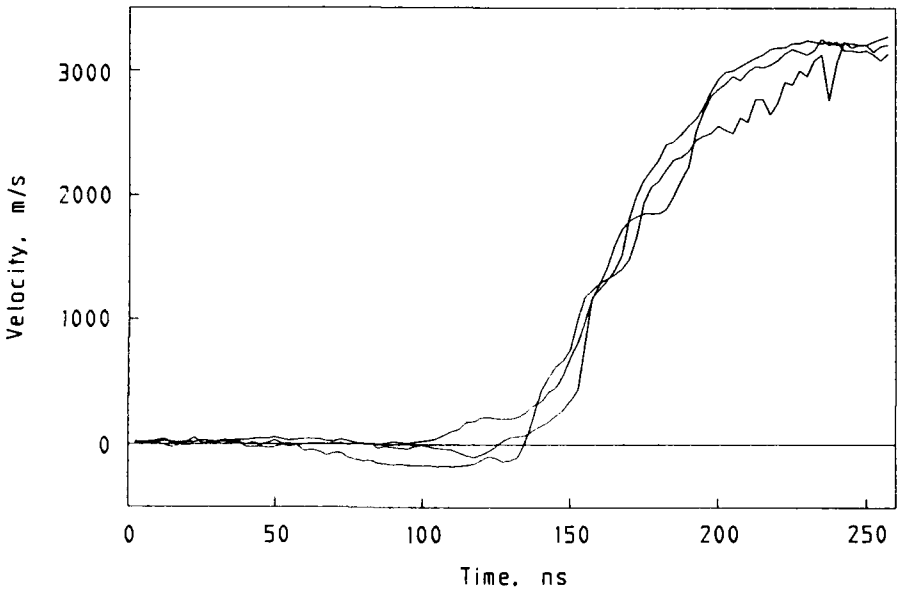

Figure 22: Velocity-time histories (25 μm flyer thickness, 0.25 mm bridge width, 2.0 kV).

5.2.2 MRL Firing Equipment

For a series of 10 tests, the flyer surfaces were treated using the miniature grit blaster, the fringe constant was 2678 m/s, and the charge voltage was 1.5 kV. The quality of the Lissajous figures varied, being either slightly better or worse, or about the same, as the one shown in Figure 16. Peak velocities of about 3900 m/s were obtained. The peak accelerations were about 100 Gm/s^2 and again the flyer travel was 0.25 mm. Further results are published elsewhere [15].

5.3 *Free-Surface Velocities*

With a target thickness of 0.49 mm and a fringe constant of 964 m/s, negative velocity-time histories with peaks of about - 850 m/s were obtained. On the assumption that lost fringes produced these results, the fringe constant was increased to 3853 m/s. The velocity-time histories then had the expected shape, i.e. a rapid rise to a peak velocity followed by a slower decay. However, as only about 1/4 of a fringe was produced, selection of the centre of the Lissajous figure was too subjective to give reliable data. Tests with the other target thicknesses gave similar results.

5.4 *PMT Anode Pulse Rise Time*

The rise times obtained for the MON, D1 and D2 PMTs were in the range 3.3 ns to 4.0 ns, 3.2 ns to 4.0 ns, and 4.5 ns to 6.4 ns respectively.

6. *Discussion*

Initially, the operation of the VISAR optics was hampered by a non-flat interference beamsplitter. The fringes produced with this beamsplitter were "saddle-shaped" rather than broad curved or "bull's-eye" type fringes. The installation of a new beamsplitter produced broader fringes which reduced the variability of the results.

While the plano-convex lens is currently preferred for the target lens, it is probably not the optimum form to use; an achromat of the same focal length would probably be better as it would have less spherical aberration. Spherical aberration means that light rays travel to the PMTs over slightly different paths and hence cause a range of Doppler shifts to occur across the PMT aperture, resulting in degradation of fringe contrast. A similar effect occurs when the return beam is decollimated by target motion. An achromat could give some worthwhile improvement in the quality of the VISAR data.

As noted at Table 2, through error, the delay mirror translation was too small (by 2.7 mm) as allowance had not been made for the effective etalon length of the $\lambda/8$ waveplate/beamsplitter combination. Thus the interferometer was not set up for optimum fringe contrast. The effect of this error on contrast would increase with decreasing etalon length.

Alignment of the laser beam with the centre of the small-scale bridge foils by means of the jeweller's eyepiece was quite difficult. Indeed, during subsequent work it was shown to be unsatisfactory, necessitating the development of a method using a microscope [15].

In normalizing the data, the monitor signal is appropriately scaled and used as a divisor. The monitor signal contains both self-light and other noise. Thus, while normalization produces more circular Lissajous figures it also results in noiser data which is most noticeable near the end of a record where the beam intensity has fallen to a low level. To minimize the effects of self-light, and for that matter other optical noise, EMI, and detector shot noise, it has been found that in this system it is best to use a high laser power (0.1 W - 0.4 W) and small

PMT apertures; 2 mm diameter apertures have been found by experience to be about optimum.

As the acceleration of the flyers increases (resulting in increased fringe frequencies), our Lissajous figures depart more from the ideal form. Thus, our best Lissajous figure is for the heavier 50 μm (1.5 mm bridge width) flyer (maximum acceleration ≈ 10 Gm/s^2) and worst for the lighter 25 μm (0.25 mm bridge width) flyer (maximum acceleration ≈ 100 Gm/s^2) and free-surface velocity measurements (reliable estimate of the maximum acceleration could not be made). This suggests that one of the likely reasons for the distorted Lissajous figures is an inadequate photodetector bandwidth. Initially, based on the highest fringe frequency observed in the signals, the bandwidth was thought to be in the range 50 MHz to 100 MHz. Later tests with the optical pulser appeared to agree with this observation. It should be noted however that the rise times obtained from the pulse tests might be slightly too high because the optical pulser was not quite fast enough to be considered a good facsimile of a delta function light source [12]. But the pulse tests do show the high frequency response of the two data PMTs to be different, which could also contribute to the distortion. Other possible reasons for the distorted Lissajous figures are discussed in the literature [13, 14, 18, 19].

Our measurements have shown that the PMTs are linear over the voltage range of interest and hence non-linearity of the photodetectors is not considered to be a problem. In addition, diffusing screens are used directly ahead of the PMTs' photocathodes to reduce target motion effects. Erroneous monitor signals can also cause problems; these errors can arise through improper alignment of the VISAR optics and photodetectors. The alignment is performed with care and we expect it to be satisfactory.

For VISAR data that produces essentially a circular Lissajous figures, error analysis suggests that the uncertainty of the calculated velocity is less than 1%. However, given that most records from this VISAR, for EBF flyer generator firings, will have some distortion, this accuracy cannot be claimed. The Lissajous figures characteristically have several circular-like loops which do not have a common centre. Hence, choosing a centre for the velocity calculation is a compromise. Some likely effects of this are as follows:

(i) The velocity-time history up to the peak will be distorted, as shown by simulated fringes in Figure 23. For flyer peak velocity measurements, this is not a serious limitation. But the acceleration-time history derived by numerical differentation of the velocity-time history will be erroneous, as shown.

(ii) The peak velocity could be in error by about 10% (Fig. 23).

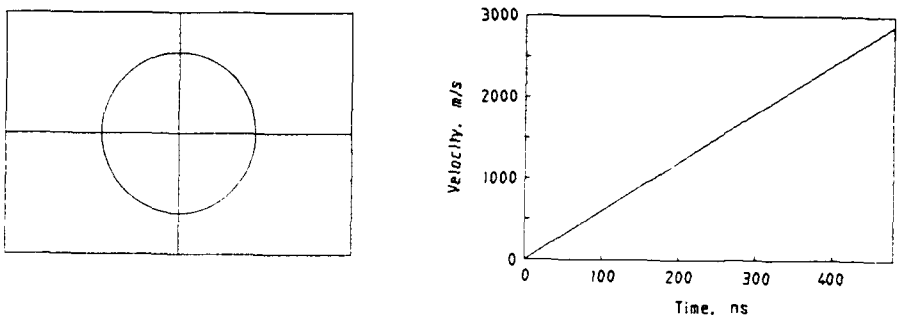

(a)

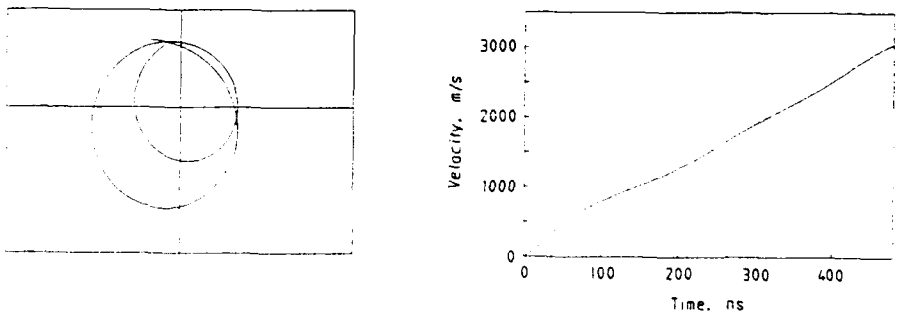

(b)

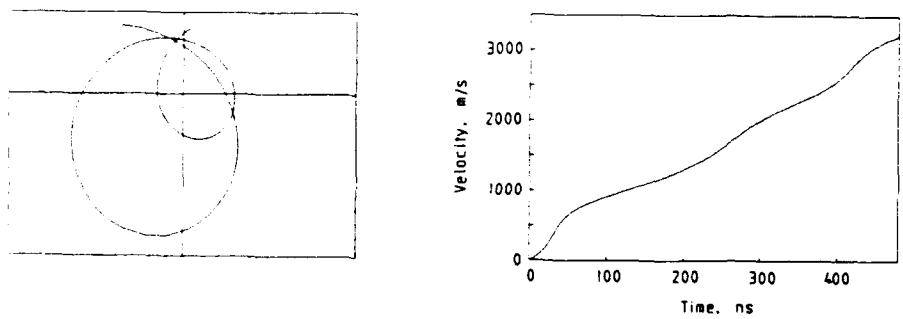

(c)

Figure 23: *Plots from simulated VISAR data (about 2 fringes) to illustrate: (a) perfect data, (b) and (c) defective data causing artificial accelerations and increasing error in the peak velocity.*

7. Conclusions

A range of tests were conducted to characterize and optimize the 3-detector VISAR system for flyer velocity measurements. During the tests, proper flyer surface treatment, target lens type, and photodetector response were found to be important. Use of a miniature grit-blaster was found to be a good method of roughening the flyer surface and, of the lens types available for evaluation, a short focal length plano-convex lens was preferred. The most likely factor limiting the performance of the VISAR system was considered to be the high-frequency response of the photodetectors which was found to be significantly less than 100 MHz.

After replacement of the VISAR's original non-flat interferometer beamsplitter, the two arms of the interferometer were no longer compensated. The VISAR velocity equation was shown to need modification to account for the effective etalon length of the beamsplitter/$\lambda/8$ waveplate combination.

We found the 3-detector VISAR system capable of making peak velocity measurements for small- and medium-scale flyers, the velocity range tested being 1500 m/s to 3900 m/s with accelerations up to about 100 Gm/s^2. However, the system would have limited value for studies where accurate acceleration-time histories are needed or for free-surface velocity measurements. The uncertainty of the peak velocities was found to be related to the form of the Lissajous figure. In general, for a good Lissajous figure the uncertainty would be about ± 2% but on the other hand would be about ± 10% for a poor Lissajous figure.

8. Acknowledgements

The technical assistance of Messrs M.V. Cleeland, B.E. Jones, K.S. Jackson, R. Klar, and G.N. Sprott, along with the advice and support of Drs D.D. Richardson and R.P. Creaser, was greatly appreciated. The author also wishes to acknowledge the valuable assistance of W.F. Hemsing (LANL) and O.B. Crump (SNL); both provided detailed information on the design and use of VISARs. The support of the USAF Armament Laboratory, Eglin AFB is also acknowledged. Recent discussions on this work with Mr P.F.X. Ryan were also helpful.

9. References

1. Barker, L.M. and Hollenbach, R.E. (1972). Laser interferometer for measuring high velocities of any reflecting surface. *Journal of Applied Physics*, Vol. 43, No. 11.

2. McMillan, C.F., Goosman, D.R., Parker, N.L., Steinmetz, L.L., Chau, H.H., Huen, T., Whipkey, R.K. and Perry, S.J. (1988).
Velocimetry of fast surfaces using Fabry-Perot interferometry. *Review of Scientific Instruments*, **59** (1).

3. Richardson, D.D. (1987).
Studies on slapper detonators (U) (MRL Report MRL-R-1083) (Confidential). Maribyrnong, Vic.: Materials Research Laboratory.

4. Richardson, D.D., Northeast, E.D. and Ryan, P.F.X. (1988).
An exploding foil flying plate generator (MRL Report MRL-R-1133). Maribyrnong, Vic.: Materials Research Laboratory.

5. Ryan, P.F.X., Jones, B.E. and Richardson, D.D. (1989).
A medium scale flying plate generator design (MRL Research Report MRL-RR-2-89). Maribyrnong, Vic.: Materials Research Laboratory.

6. Hemsing, W.F. (1979).
Velocity sensing interferometer (VISAR) modification. *Review of Scientific Instruments*, **50** (1).

7. Barker, L.M. (1968).
Fine structure of compressive and release wave shapes in aluminium measured by the velocity interferometer technique. *Behaviour of dense media under high dynamic pressures*. New York: Gordon and Breech.

8. Barker, L.M. and Hollenbach, R.E. (1970).
Shock-wave studies of PMMA, fused silica and sapphire. *Journal of Applied Physics*, Vol. 41, No. 10.

9. Barker, L.M. and Schuler, K.W. (1974).
Correction to the velocity-per-fringe relationship for the VISAR interferometer. *Journal of Applied Physics*, Vol. 45, No. 8.

10. Clifton, R.J. (1970).
Analysis of the laser velocity interferometer. *Journal of Applied Physics*, Vol. 41, No. 13.

11. Drain, L.E. (1980).
The laser Doppler technique. John Wiley & Sons.

12. McHose, R.E.
Time characteristics of photomultipliers – some general observations. RCA Application Note AN-4884.

13. Hemsing, W.F. (1989).
Comment on VISAR analysis in the presence of large intensity changes: Application to the expanding ring. *Review of Scientific Instruments*, **60** (12).

14. Hemsing, W.F. (1983).
VISAR : 2½ minutes for data reduction. *SPIE Vol. 427 – High speed photography, videography and photonics.*

15. Hatt, D.J. and Waschl, J.A. (1991).
Performance evaluation of an EBF generated thin flyer plate (MRL Technical Report MRL-TR-91-28). Maribyrnong, Vic.: Materials Research Laboratory.

16. Masinskas, J.J. and Richardson, D.D. (1987).
A miniature high voltage power supply for slapper detonators (U) (MRL Report MRL-R-1093). Maribyrnong, Vic.: Materials Research Laboratory.

17. Keeler, R.N. and Royce, E.B. (1970).
Six lectures on shock-wave physics (UCRL-71846). California: Lawrence Radiation Laboratory.

18. Gourdin, W.H. (1989).
VISAR analysis in the presence of large intensity changes: Application to the expanding ring. *Review of Scientific Instruments*, **60** (4).

19. Gourdin, W.H. (1989).
Reply to comment on VISAR analysis in the presence of large intensity changes: Application to the expanding ring [Review of Scientific Instruments, 60, 3832, 1989]. *Review of Scientific Instruments*, **60** (12).

Appendix A

Derivation of VISAR Equation

Referring to the diagram shown in Figure A1, for zero optical path difference the path lengths of the imaginary interferometer must be equal. When a $\lambda/8$ waveplate is added to the non-delay arm, in order to obtain good fringe visibility with spatially incoherent light mirror M_{ND} would need to be translated by

$$l_p\left(1 - \frac{1}{n_p}\right) \tag{A.1}$$

where

l_p = thickness of the $\lambda/8$ waveplate, and
n_p = refractive index of the $\lambda/8$ waveplate.

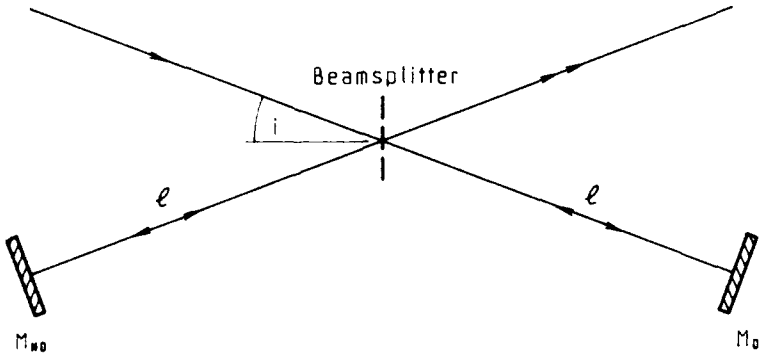

Figure A1: *Imaginary interferometer arrangement used for derivation of the VISAR velocity equation. Arm length, l, is approximately 290 mm.*

Thus, the new optical path length for this arm would be

$$l - l_p + n_p l_p + l_p\left(1 - \frac{1}{n_p}\right) = l + l_p\left(n_p - \frac{1}{n_p}\right) \qquad \text{(A.2)}$$

where l = initial arm length. Similarly, allowing for the thickness of the beamsplitter, the new delay arm optical path length would be

$$l - l_b' + n_b l_b' + l_b'\left(1 - \frac{1}{n_b}\right) = l + l_b'\left(n_b - \frac{1}{n_b}\right) \qquad \text{(A.3)}$$

where

n_b = retractive index of the beamsplitter,
l_b = thickness of the beamsplitter,
$l_b' = \dfrac{l_b}{\cos r} = \dfrac{l_b}{\cos\left[\sin^{-1}(\sin i / n_b)\right]}$,
i = angle of incidence, and
r = angle of refraction.

Then, to obtain white light fringes, zero optical path difference is again needed and therefore mirror M_D would need to be translated by Δl so that

$$\Lambda_1 = 0 = 2\left[l + l_p\left(n_p - \frac{1}{n_p}\right)\right] - 2\left[l + l_b'\left(n_b - \frac{1}{n_b}\right) + \Delta l\right] \qquad \text{(A.4)}$$

$$\text{and} \quad \Delta l = l_p\left(n_p - \frac{1}{n_p}\right) - l_b'\left(n_b - \frac{1}{n_b}\right) \qquad \text{(A.5)}$$

Now let

$$l_{air}\left(n_a - \frac{1}{n_a}\right) = \Delta l \qquad \text{(A.6)}$$

or

$$l_{eff} = \frac{\Delta l}{(n_e - 1/n_e)} \tag{A.7}$$

This expression gives the effective etalon length, l_{eff}, for the $\lambda/8$ waveplate/beamsplitter combination.

From the white light fringe position, mirror M_D is initially translated back by Δl and then by $x = l_e\,(1 - 1/n_e)$ after an etalon is added. These translations ensure good fringe contrast with spatially incoherent light. Thus, the optical path difference is now

$$\Lambda_2 \neq 0 = 2\left[l + l_p\left(n_p - \frac{1}{n_p}\right)\right] - 2\left[l + l_b'\left(n_b - \frac{1}{n_b}\right) - l_e + n_e l_e + l_e\left(1 - \frac{1}{n_e}\right)\right] \tag{A.8}$$

$$= 2\left[l_p\left(n_p - \frac{1}{n_p}\right) - l_b'\left(n_b - \frac{1}{n_b}\right) - l_e\left(n_e - \frac{1}{n_e}\right)\right] \tag{A.9}$$

From (A.5) and (A.6) this gives

$$\Lambda_2 = 2\left[l_{eff}\left(n_e - \frac{1}{n_e}\right) - l_e\left(n_e - \frac{1}{n_e}\right)\right] \tag{A.10}$$

$$\therefore \Lambda_2 = 2\,(l_{eff} - l_e)\left(n_e - \frac{1}{n_e}\right) \tag{A.11}$$

Thus the phase difference will be

$$\phi_0 = \frac{2\pi}{\lambda_0}\,\Lambda_2 \tag{A.12}$$

$$= \frac{2\pi}{\lambda_0} 2\,(l_{eff} - l_e)\left(n_e - \frac{1}{n_e}\right) \tag{A.13}$$

In the arrangement of the Michelson interferometer used for length measurements, Λ_2 is changed thereby causing fringe shifts. On the other hand, in the velocity interferometer λ_0 is changed to cause fringe shifts. Light reflected from a surface moving with velocity u will sustain a double Doppler shift [11] so that

$$\Delta\lambda = -2\lambda_0 \frac{u}{c} \tag{A.14}$$

$$\lambda = \lambda_0 + \Delta\lambda \tag{A.15}$$

$$= \lambda_0\left(1 - 2\frac{u}{c}\right) \tag{A.16}$$

and the phase difference will then be

$$\phi = \frac{2\pi}{\lambda_0(1 - 2u/c)} 2\,(l_{eff} - l_e)\left(n_e - \frac{1}{n_e}\right) \tag{A.17}$$

Thus, the phase change is

$$\phi_0 - \phi = \frac{2\pi}{\lambda_0} 2\,(l_{eff} - l_e)\left(n_e - \frac{1}{n_e}\right) - \frac{2\pi}{\lambda_0(1 - 2u/c)} 2\,(l_{eff} - l_e)\left(n_e - \frac{1}{n_e}\right) \tag{A.18}$$

$$= \frac{4\pi}{\lambda_0}(l_{eff} - l_e)\left(n_e - \frac{1}{n_e}\right)\left[1 - \frac{1}{(1 - 2u/c)}\right] \tag{A.19}$$

$$\text{The total fringe shift} = F = \frac{\phi_0 - \phi}{2\pi} \tag{A.20}$$

$$\therefore F = \frac{2}{\lambda_0}(l_{eff} - l_e)\left(n_e - \frac{1}{n_e}\right)\left[1 - \frac{1}{(1 - 2u/c)}\right] \qquad \text{(A.21)}$$

Rearranging

$$\frac{\lambda_0 F}{2(l_{eff} - l_e)(n_e - 1/n_e)} = \frac{(1 - 2u/c) - 1}{(1 - 2u/c)} = \frac{-2u}{c(1 - 2u/c)} \approx \frac{-2u}{c} \qquad \text{(A.22)}$$

Thus

$$u \approx \frac{\lambda_0 c F}{4(l_e - l_{eff})(n_e - 1/n_e)} \qquad \text{(A.23)}$$

This equation requires a correction factor due to the optical dispersion of the etalon material [9], so that

$$u \approx \frac{\lambda_0 c F}{4(l_e - l_{eff})(n_e - 1/n_e)(1 + \delta)} \qquad \text{(A.24)}$$

where δ = optical dispersion correction.

For the MRL VISAR,

n_b = 1.462 (fused silica, λ = 514.5 nm)
n_p = 1.55 (crystalline quartz, λ = 514.5 nm)
l'_b = 9.173 mm
l_p = 4.895 mm

From (A.5) and (A.7)

l_{eff} = - 3.48 mm

Appendix B

Translation of the Delay-Arm Mirror

Assume the mirror in the delay arm is located at B as shown in Figure A2 prior to insertion of the etalon. After the etalon of length l_e is inserted, it is required that the mirror is translated so that the ray shown returns to the beamsplitter along the same path. Thus, the mirror needs to be translated by the distance

$$x = CB + CD \tag{B.1}$$

Noting that

$$AO = CE + EF \tag{B.2}$$

and since

$$\tan r = \frac{EF}{l_e} \tag{B.3}$$

$$AO = CE + l_e \tan r \tag{B.4}$$

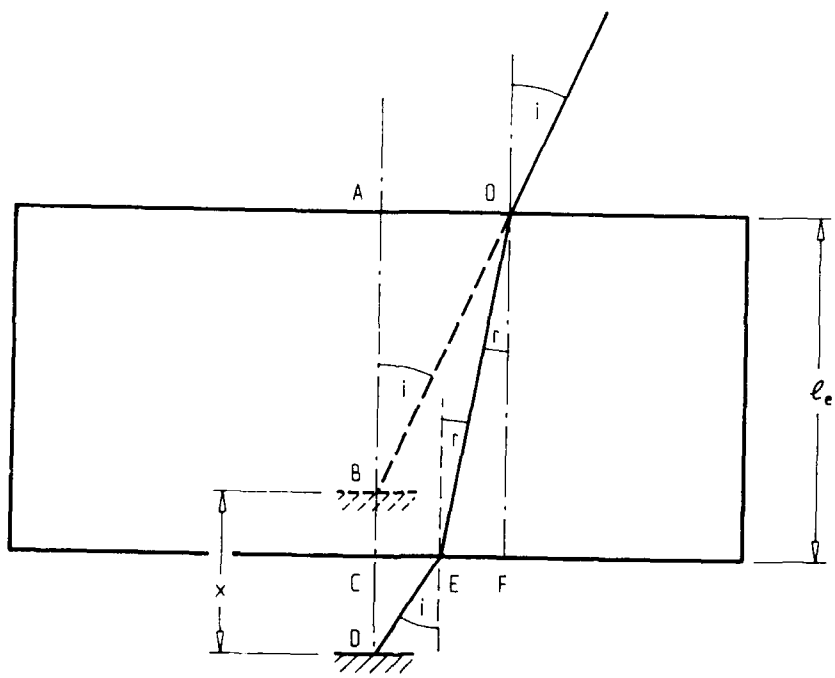

Figure A2: Translation of the delay-arm mirror after insertion of an etalon.

Now

$$\tan i = \frac{CE}{CD} = \frac{AO}{AB} \tag{B.5}$$

so that

$$AO = CD \tan i + l_e \tan r \tag{B.6}$$

$$= (x - CB) \tan i + l_e \tan r \tag{B.7}$$

From (B.5) and (B.7)

$$AB \tan i = (x - CB) \tan i + l_e \tan r \tag{B.8}$$

or

$$(l_e - CB) \tan i = (x - CB) \tan i + l_e \tan r \tag{B.9}$$

Therefore

$$l_e \tan i = x \tan i + l_e \tan r \tag{B.10}$$

from which

$$x = l_e \left(1 - \frac{\tan r}{\tan i}\right) \tag{B.11}$$

From Snell's law

$$n = \frac{\sin i}{\sin r} \tag{B.12}$$

thus

$$x = l_e\left(1 - \frac{1}{n}\,\frac{\cos i}{\cos r}\right) \tag{B.13}$$

and since i is small

$$x \approx l_e\left(1 - \frac{1}{n}\right) \tag{B.14}$$

Appendix C

Beam Intensity as a Function of Target Motion

Let I_0 = the irradiance of a perfectly collimated return beam, and I = the irradiance at distance S of a decollimated return beam, this being due to target motion Δx (Fig. A3). Then, assuming the same amount of light from the target enters the lens,

$$I = I_0 \left(\frac{d_f}{d_u}\right)^2 \tag{C.1}$$

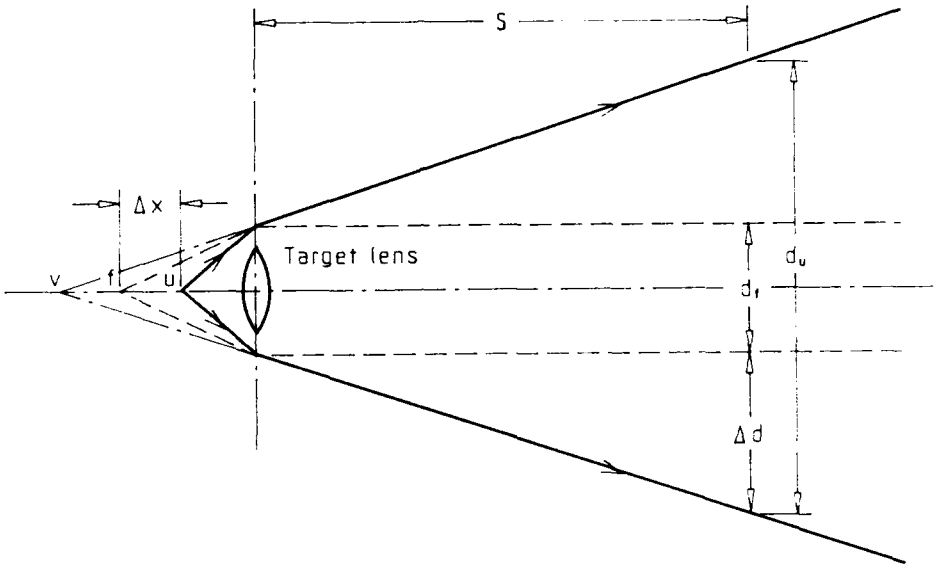

Figure A3: Change in intensity of return beam due to target motion.

Since

$$d_u = d_f + 2\Delta d, \tag{C.2}$$

$$\frac{1}{f} = \frac{1}{u} - \frac{1}{v}, \tag{C.3}$$

and

$$\frac{d_t}{2v} = \frac{\Delta d}{S} \tag{C.4}$$

we obtain

$$I = \frac{1}{[1 + S\,(1/u - 1/f)]^2}\, I_0 \tag{C.5}$$

Now

$$u = f - \Delta x \tag{C.6}$$

so that

$$I \approx \frac{1}{(1 + S\Delta x/f^2)^2}\, I_0 \tag{C.7}$$

Appendix D

Data Processing and Reduction

Referring to Figure A4 the D1 and D2 data signals can be represented in terms of intensity by two-beam interference equations as follows:

For D1:

$$I_s = I + I_i + 2I\sqrt{RT}\cos\phi \qquad \text{(D.1)}$$

For D2:

$$I_p = I + I_i + 2I\sqrt{RT}\cos(\phi - \beta) \qquad \text{(D.2)}$$

where

I_s	=	intensity of the *s*-polarized recombined beam,
I_p	=	intensity of the *p*-polarized recombined beam,
I	=	intensity of the coherent beam entering the interferometer,
I_i	=	intensity of the incoherent beam entering the interferometer,
R	=	fraction of reflected beam,
T	=	fraction of transmitted beam,
ϕ	=	phase difference between recombined coherent beams, and
ß	=	phase difference between the *s*- and *p*-polarized beams.

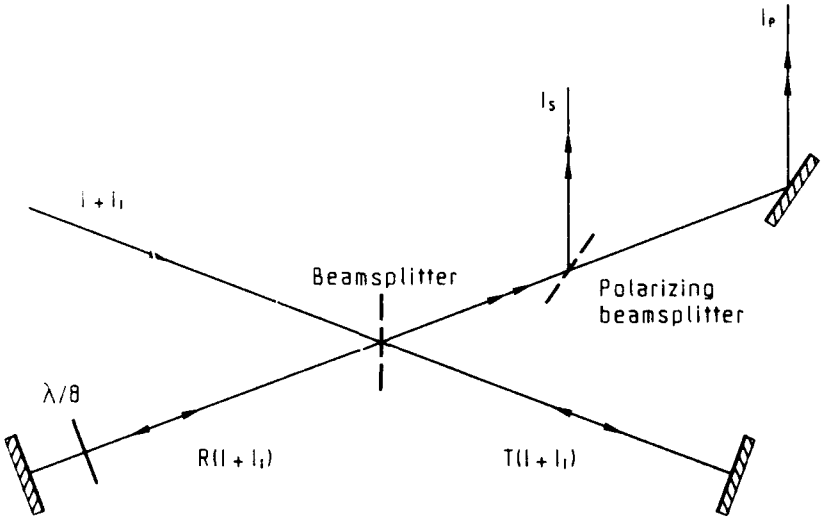

Figure A4: *Interferometer showing division of incoming light, $I + I_i$, into reflected and transmitted components.*

Put

$$\gamma I_m = I + I_i \tag{D.3}$$

where

I_m = intensity of the monitor beam, and
γ = scaling factor (Beam Intensity Factor).

Subtracting (D.3) from (D.1) and (D.2) gives

$$I_s' = 2I\sqrt{RT}\cos\phi \tag{D.4}$$

$$I_p' = 2I\sqrt{RT}\cos(\phi - \beta) \tag{D.5}$$

These signals can be used to calculate the velocity-time history using the artangent algorithm [6, 14]:

$$u = \frac{K}{2\pi}\tan^{-1}\left(\frac{1}{\sin\beta}\frac{I_p'}{I_s'} - \cot\beta\right) \tag{D.6}$$

However, the beam intensity varies significantly during tests with exploding bridge foil flyer generators, causing corresponding variations in the $2I\sqrt{RT}$ term, i.e. the Lissajous figure is likely to be a circular spiral. As choosing a centre for a spiral is difficult, the data are normalized as follows:

Dividing (D.4) and (D.5) by (D.3) gives

$$I_{Ns} = \alpha\cos\phi \tag{D.7}$$

and

$$I_{Np} = \alpha\cos(\phi - \beta)$$

where

$$\alpha = \frac{2\sqrt{RT}}{1 + I_i/I}$$

For small- and medium-scale EBF flyer generators, use of a fairly high laser power (0.1 W - 0.3 W) ensures that $I > I_i$ thereby making α approximately constant. This then results in a more circular Lissajous figure which aids manual centering by the operator.

SECURITY CLASSIFICATION OF THIS PAGE **UNCLASSIFIED**

DOCUMENT CONTROL DATA SHEET

REPORT NO.	AR NO.	REPORT SECURITY CLASSIFICATION
MRL-TR-91-42	AR-006-841	Unclassified

TITLE

A VISAR velocity interferometer system at MRL for slapper detonator and shockwave studies

AUTHOR(S)
David J. Hatt

CORPORATE AUTHOR
Materials Research Laboratory
PO Box 50
Ascot Vale Victoria 3032

REPORT DATE	TASK NO.	SPONSOR
December, 1991	DST 90/146	DSTO

FILE NO.	REFERENCES	PAGES
G6/4/8-4051	19	50

CLASSIFICATION/LIMITATION REVIEW DATE

CLASSIFICATION/RELEASE AUTHORITY
Chief, Explosives Ordnance Division

SECONDARY DISTRIBUTION

Approved for public release

ANNOUNCEMENT

Announcement of this report is unlimited

KEYWORDS

3 detector VISAR	Exploding Bridge Foil Generators	Flyer Plates
Velocity-Time Histories		

ABSTRACT

This report describes the commissioning and appraisal of a conventional 3-detector VISAR velocity interferometer system (Systems, Science, and Software, Model 3SLVI-401) for measuring the velocity-time histories of small plastic flyer plates produced by exploding bridge foil generators.

Proper treatment of the flyer surface to diffusely reflect the laser beam was found to be important. Roughening the surface with a miniature grit-blaster produced the best results. Peak velocities in the range 1500 m/s to 3900 m/s were obtained for small- and medium-scale flyers (bridge widths of 0.25 mm and 1.5 mm, respectively). Accelerations were in the range 10 Gm/s^2 to 100 Gm/s^2. The uncertainty of the measurements was found to be related to the limited high-frequency response (less than 100 MHz) of the photodetectors.

After replacement of the original non-flat beamsplitter, the arms of the interferometer were not quite compensated. A modified VISAR velocity equation that allows for the effective etalon length of the $\lambda/8$ waveplate/beamsplitter combination is derived.